Modeling Interplanetary Expansion and Deformation of CMEs with ANTEATR-PARADE II: Sensitivity to Input Parameters

C. Kay[1,2], T. Nieves-Chinchilla[1]

[1]Heliophysics Science Division, NASA Goddard Space Flight Center, Greenbelt, MD, USA
[2]Dept. of Physics, The Catholic University of America, Washington DC, USA

Key Points:

- CME predictions depend on many input parameters and the exact sensitivity varies with CME scale
- As the scale increases from slow to extreme drag forces become more important than the drag force
- CME mass, velocity, cross-sectional size, and magnetic field properties cause the largest changes.

Corresponding author: Christina Kay, ckay@gmail.com

Abstract

Space weather predictions related to coronal mass ejections (CMEs) requires understanding how a CME is initiated and how its properties change as it propagates. While some parameters can be measured relatively easily near the Sun, others are much harder to disentangle from projected coronagraph images. Most predictions have been limited to the arrival time of a CME and include little to no information about the CME's internal properties. ANTEATR-PARADE represents the most thorough description of the interplanetary evolution of CMEs in a highly computationally-efficient model. (Kay & Nieves-Chinchilla, 2020) presents the derivation of this model, where we have added an elliptical cross section to the original arrival time model ANTEATR and introduced internal magnetic forces that, combined with the drag, can alter the shape of the central axis and cross section. ANTEATR-PARADE results include the transit time of CMEs, as well as the shape and size, propagation and expansion velocities, density, and magnetic field properties upon impact. We determine the dependence of each output on each of the ANTEATR-PARADE input parameters. For a fast CME, we see that the transit time and propagation velocity depend most strongly on inputs that modify the drag force whereas the inputs affecting the magnetic forces determine the expansion of the CME. We extend to other CMEs and find that the sensitivities change with CME scale. Magnetic forces become more important for an average CME whereas the drag force becomes more important for an extreme CME.

Plain Language Summary

Frequently, in a violent explosion of mass, energy, and magnetic field the Sun sheds part of its atmosphere as a transient that propagates out through the solar system. These CMEs, continue evolving, expanding and distorting as they interact with their surroundings. We have developed a model that includes the effects of the forces from a CME's magnetic field and the external drag forces, which will cause the size and shape of the CME to change over time. Our model determines how long it would take for a CME to reach Earth, the speed at which it will propagate and expand, how long it will take to pass the Earth, and what it's magnetic field strength and density will be at the time of impact. This model depends on many input parameters, some of which can be easily measured in the corona and others that are much harder to constrain. We determine how the uncertainties in each input affects each output. We find that the behavior differs as the scale of the CME changes from a common, average CME to a rare, highly energetic, extreme CME. Average CMEs tends to be more sensitive to the magnetic forces and extreme CMEs to the drag forces.

1 Introduction

Frequently, in a violent explosion of mass, energy, and magnetic field the Sun sheds part of its atmosphere as a transient that propagates out through the solar system. These CMEs, continue evolving, expanding and distorting as they interact with their surroundings. A CME can cause severe space weather effects when its path causes it to impact another object. Close to home, the interaction between a CME and the Earth's magnetic field can lead to stunning aurora but also adversely affect human technologies, both in space and at the surface (e.g Baker, 2000; Schrijver, 2015). Farther away, CMEs can interact with missions throughout the solar system. Predicting the behavior of CMEs will become increasingly important as humans look toward future exploration of the moon and Mars. Understanding the impact of a CME requires knowing what that CME was like as it was initiated near the Sun, and how it changes while en route.

If a CME's properties are observed near the Sun then we can make predictions on when it may arrive at Earth and what its properties may be at the time of impact. Most predictions have focused solely on the arrival time as CMEs as the simplest estimate of it only requires the propagation speed of the CME. Most arrival time models simulate some form of drag force causing the CME speed to gradually approach that of the background solar wind (e.g. Vršnak et al., 2013; Hess & Zhang, 2015; Möstl et al., 2015), though machine learning techniques present an opportunity for relatively accurate predictions without simulating the underlying physics (e.g Liu et al., 2018). Alternatively, complex magnetohydrodynamic (MHD) simulations can be used to simultaneously model most aspects of a CME, including arrival times and properties upon impact (e.g Odstrcil et al., 2004; Jin et al., 2017; Pomoell & Poedts, 2018), but these rarely run on the time scales necessary for space weather predictions.

While over the years arrival time predictions have improved, recent results seem to have stagnated with a mean absolute error of about 10 hours (e.g. Riley et al., 2018; Wold et al., 2018). The quality of predictions depends not only on the quality of the models themselves, but also the inputs used to initiate the model. Multidimensional drag models depend on the CME's relative location to the impact object. A measurement of position can be estimated from a single coronagraph image (e.g. Xie et al., 2004; Xue et al., 2005). The accuracy improves when multiple images from different viewpoints are combined using various geometric reconstruction techniques but there is often still a discrepancy between the results of different techniques or different users fitting the same CME (Mierla et al., 2010, and references within). While we do not have "true" positions for real CMEs, this sensitivity has long been seen and a team was formed through the International Space Science Institute to explicitly demonstrate it(Verbeke et al., 2019). The team has demonstrated the improvement in measured positions with multiple viewpoints and show the effect on CME arrival time predictions using synthetic coronagraph images with known CME positions fit by numerous experts in CME reconstruction (Verbeke et al. 2021, in prep).

The severity of a CME impact at Earth depends directly on the magnetic field strength and orientation, but few models have made an attempt to model this in a manner suitable for space weather predictions. The magnetic field strength requires knowing the initial values near the Sun, which can be estimate or inferred (e.g. Gopalswamy et al., 2017) but is not routinely done for all eruptions. Magnetic field strength predictions also require knowing how the CME volume evolves during propagation. The orientation requires knowing the handedness of a CME's internal flux rope and the general orientation of the CME, which is hard to measure, even in multi-viewpoint observations (Nieves-Chinchilla et al., 2012; Chi et al., 2018). Often the orientation of a CME reconstructed in situ differs significantly from the orientation inferred in the coronal (Al-Haddad et al., 2018), and it is unclear whether this represents an evolution of the CME or simply uncertainties in both measurements. Kunkel and Chen (2010), Savani et al. (2015) and Kay et al. (2017) represent the only efforts to produce in situ magnetic profiles by forward modeling a CME's internal magnetic field. The positional information inferred from the corona orients a simple flux rope that propagates over a synthetic observer. These model show promise for magnetic field predictions, but are not yet actively used for such.

To further complicate interplanetary propagation, models suggest that the shape of a CME can change during interplanetary propagation. Specifically, the cross section tends to become more elliptical with the width decreasing relatively in the direction of propagation (Riley & Crooker, 2004; M. J. Owens et al., 2005). This deformation is typically referred to as "pancaking" and, while not directly measured, can also be inferred from other in situ observations (e.g. Russell & Mulligan, 2002; M. Owens & Cargill, 2004). Isavnin (2016) develop a much more complex flux rope model that incorporates pancaking and other deformations through additional free parameters. This flux rope model can much more accurately reproduce observed in situ profiles, but it remains to be seen whether the inputs can suitably determined for predictions.

One approach to handling a large amount of uncertainties in the initial parameters is to run ensemble studies sampling the range of those uncertainties. This yields not only the most probable results, but also a measure of the uncertainty of each output. To do this on the time scales needed for predictions requires very computationally-efficient models. Many of the simple, physics-driven drag models are suitable and have been adapted for ensemble simulations (e.g. Dumbović et al., 2018; Amerstorfer et al., 2018). The Open Solar Physics Rapid Ensemble Information (OSPREI) suite of models combines a model for the coronal deflection and rotation of CMEs (Kay et al., 2015), with an arrival time model (Kay & Gopalswamy, 2018), and an in situ magnetic field model (Kay et al., 2017). Through the use of ensembles, Kay and Gopalswamy (2018) showed how uncertainties in the CME properties used to initiate the coronal simulation can propagate through the chain of simulations can affect the output parameters related to space weather predictions such as travel time and magnetic field strength and orientation.

In Kay and Nieves-Chinchilla (2020), hereafter Paper 1, we took the simple arrival time model ANTEATR (ANother Type of Ensemble Arrival Time Results, Kay & Gopalswamy, 2018; Kay et al., 2020) and expanded it to ANTEATR-PARADE (Physics-driven Approach to Realistic Axis Deformation and Expansion). We included magnetic forces that, combined with the drag forces, act to change the shape and size of a CME's central axis and cross section during its interplanetary propagation. Paper I evaluated the relative importance of the different components of the magnetic forces and drag force and found that the drag tends to have the strongest effect. We also found that the final results are quite sensitive to the method by which the initial velocity of the CME front is broken down into propagation and expansion speeds. The primary focus of Paper I is presenting the model details and some initial results. In this paper we fully explore the sensitivity of ANTEATR-PARADE results to all of its inputs and infer how these sensitivities could affect space weather predictions.

2 ANTEATR-PARADE Model

ANTEATR-PARADE is a detailed, interplanetary CME propagation model based on the ensemble arrival time model ANTEATR (Kay & Gopalswamy, 2018; Kay et al., 2020). Here we briefly describe the details of ANTEATR-PARADE, for the full details see Paper I. ANTEATR-PARADE uses both internal magnetic and external drag forces to determine the expansion, deformation, and deceleration of a CME as it propagates away from the Sun. The expansion determines the CME size, which is defined by the total angular width, AW, and the angular width of the cross section, $AW_{\perp}$. Unlike the original ANTEATR, both the toroidal axis and the cross section can have an elliptical shape. We describe the shape using δ_{Ax}, the ratio of the length of the axis in the radial direction to it's length in the perpendicular direction, δ_{CS}, the ratio of the cross-sectional width in the radial direction to its width in the perpendicular direction, **and δ_{CA}, the ratio of the width of the cross section in the radial direction to the width of the axis in the perpendicular direction.** Asymmetric forces, either drag or magnetic, can cause the δs to change. The CME's internal magnetic field evolves from its initial values via flux conservation. As such, ANTEATR-PARADE not only yields the transit time of CMEs, but the shape and size, propagation and expansion velocities, density, and magnetic field properties upon impact. These values can also be use to derive parameters such as the in situ duration or estimated Kp index.

For the magnetic forces, ANTEATR-PARADE calculates both magnetic pressure gradients and magnetic tension forces from the CME's toroidal and poloidal magnetic field. The magnetic pressure gradient from the toroidal magnetic field acts to expand the CME cross section and the magnetic tension from the poloidal magnetic field restricts this expansion. The tension from the toroidal magnetic field points toward the Sun whereas the hoop force resulting from the pressure gradient of poloidal magnetic field along a curved flux rope pushes away from the Sun. We find that typically, the magnetic forces cause expansion of the cross section and that for the axis the inward toroidal tension exceeds the outward hoop force. Assuming a CME moving faster than the background solar wind, the drag forces act to slow down both the radial propagation and expansion of the CME. Paper I shows that the drag forces tend to be more important than the magnetic forces, but both are important.

Calculating magnetic forces requires some sort of internal magnetic field model for the CME's flux rope. ANTEATR-PARADE uses the elliptic-cylindrical model from Nieves-Chinchilla et al. (2018), hereafter referred to as the EC model. This model results from solving Maxwell's equations in an elliptical coordinate system, making it highly suited to a CME flux rope with an elliptical cross section. The EC model represents the toroidal and poloidal current densities as a sum of polynomial terms that depend on r, the radial distance from the cross section center, which can then be used to derive the magnetic field terms. In practice, this is simplified to a single term for each current density, represented by a pair of polynomial orders $[m,\, n]$. The EC magnetic field components are

$$
\begin{aligned}
B_r &= 0 \\
B_t &= \delta_{CS} B_0 [\tau - \bar{r}^{n+1}] \\
B_p &= -\delta_{CS} h \frac{n+1}{\delta_{CS}^2 + m + 1} \frac{B_0}{C_{nm}} \bar{r}^{m+1}
\end{aligned} \tag{1}
$$

where B_0 scales both components of the magnetic field, τ and C_{nm} control the relative scaling of the toroidal and poloidal magnetic field, and h is $\sqrt{\delta_{CS}^2 \sin^2\psi + cos^2\psi}$, where ψ is the angular parameterization of cross section's elliptical shape. The radial term, B_r is zero, the toroidal field, B_t varies with distance from the center, and the poloidal field, B_p, varies with both cross section distance and angle. Nieves-Chinchilla et al. (2018) use $[m,\, n]$ = [0,1], which reduces the expression to

$$
\begin{aligned}
B_t &= \delta_{CS} B_0 [\tau - \bar{r}^2] \\
B_p &= -\frac{2\delta_{CS} h}{\delta_{CS}^2 + 1} \frac{B_0}{C_{10}} \bar{r}
\end{aligned} \tag{2}
$$

. Currently ANTEATR-PARADE only works with $[m,\, n]$ = [0,1] but future versions will incorporate other polynomial orders. Florido-Llinas et al. (2020) study the stability of the EC model for various combinations of $[m,\, n]$ and find that combinations of low τ and C leads to flux ropes that are kink unstable. The forces derived in Paper I show that this parameterization of the magnetic field leads magnetic forces that are symmetric in ψ and cannot cause any change in the CME shape, only uniform expansion or contraction.

3 Initial Velocity Decomposition

Paper I considered two different methods for converting the initial velocity of the CME front into individual bulk and expansion velocities, what we refer to as the initial velocity decomposition (IVD). If we assume that the CME is simply convected out then all components move at the same speed in the local radial direction and the angular widths remain constant. This approach has been used previously to describe CME velocities in pancaking studies as it naturally leads to the radial width becoming proportionally smaller than the perpendicular extent (e.g Riley & Crooker, 2004; M. J. Owens et al., 2005). Adding an internal overpressure, such as in M. J. Owens et al. (2005), slows down the rate at which the CME pancakes. For Paper I, we considered the extreme limit of a fully convective IVD for both the cross section and toroidal axis expansion. All velocities can then be derived from the front velocity, v_F, AW, and $AW_\perp$.

$$
\begin{aligned}
v_B &= v_F \cos AW \\
v_E &= v_F \sin AW \\
v_{CS,r} &= v_F (1 - \cos AW_\perp)
\end{aligned}
$$

$$
\begin{aligned}
v_{CS,\perp} &= v_F \sin AW \\
v_{Ax,r} &= v_F(\cos AW_\perp - \cos AW) \\
v_{Ax,\perp} &= v_E - \alpha v_{CS,r}
\end{aligned} \tag{3}
$$

v_B is the bulk velocity of the center of the CME in the radial direction (motion of the red dot labeled 'C' in Fig. 1 of Paper I). $v_{Ax,i}$ are the speeds of the axis away from the center in the radial and perpendicular directions. $v_{CS,i}$ are the expansion velocities of the cross section in the radial and perpendicular directions. The front speed v_F is the sum of v_B, $v_{Ax,r}$, and $v_{CS,r}$. Analogously, the speed of the edge in the perpendicular direction, v_E, is the sum of $v_{Ax,perp}$ and $v_{CS,r}$, but with a geometric factor α **that depends on δ_{CA}.**

In many cases, however, we found that a fully convective IVD produces CMEs that are far too thin, leading to excessively high values for any parameters that depend on flux conservation. Alternatively, we can use a fully self-similar IVD where both the angular widths and the CME shape remain constant. With this approach, if a velocity describes the change in some length L when the CME front is at a radial distance R_F, then it will vary proportionally with v_F as L/R_F. For axial lengths as L_r and $L_\perp$ and cross sectional widths r_r and $r_\perp$ we find

$$
\begin{aligned}
v_B &= v_F \left(1 - \frac{r_r + L_r}{R_F}\right) \\
v_E &= v_F + v_{Ax,\perp} + \alpha v_{CS,r} \\
v_{CS,r} &= v_F \left(\frac{r_r}{R_F}\right) \\
v_{CS,\perp} &= v_F \left(\frac{r_\perp}{R_F}\right) \\
v_{Ax,r} &= v_F \left(\frac{L_r}{R_F}\right) \\
v_{Ax,\perp} &= v_F \left(\frac{L_\perp}{R_F}\right)
\end{aligned} \tag{4}
$$

where all lengths can be determined from R_F and the AWs and δs.

Whereas the convective IVD only depends on the initial size of the CME and α, the self-similar approach depends strongly on the shape. When used to initiate ANTEATR-PARADE, the convective IVD will produce pancaking without any additional force but by definition the self-similar IVD cannot. We suspect that neither limit is the appropriate IVD for real CMEs, that the initial velocities fall somewhere in between rather than at either limit. Accordingly, we develop a method to pick an IVD that combines the values from the two limits.

In general, if we assume AW and $AW_\perp$ are constant, as we do for both cases, then we can determine $v_{CS,\perp}$ if we know the speed at which the toroidal axis moves out radially, which is $v_B + v_{Ax,r}$. Knowing $v_B + v_{Ax,r}$ also gives $v_{CS,r}$ from v_F. The other velocities cannot be determined without additional information. If we also know v_B alone then v_E follows from AW, which, with $v_{CS,r}$ then determines $v_{Ax,\perp}$.

We define two parameters f_1 and f_2 that allow $v_{Ax} = v_{Ax,r}+v_B$ and v_B to vary between their fully self-similar (f=0) and fully convective (f=1) values. Expressing the convective self-similar velocities in terms of AWs and δs we find

$$\frac{v_{Ax}}{v_F} = f_1 \cos AW_\perp + (1 - f_1)\frac{1}{1 + \delta_{CS} \tan AW_\perp} \tag{5}$$

and

$$\frac{v_B}{v_F} = f_2 \cos AW + (1 - f_2)\left[1 - \frac{\delta_{CS} \tan AW_\perp (1 + \delta_{Ax}/\delta_{CA})}{1 + \delta_{CS} \tan AW_\perp}\right] \tag{6}$$

Table 1. Range of Varied Input Parameters

	Seed	Range
M_{CME}	10^{16} g	5×10^{15} - 1.5×10^{16} g
v_{Front}	1250 km/s	750-1750 km/s
AW	45°	35-55°
$AW_{\perp}$	10°	5-15°
δ_{CS}	1	0.5-1
δ_{Ax}	0.7	0.5-0.9
δ_{CA}	0.333	0.167-0.5
C_d	1	0.5-1.5
f_1	0.5	0-1
f_2	0.5	0-1
v_{SW}	440 km/s	330-550 km/s
n_{SW}	6.9 cm^{-3}	5.175-8.625 cm^{-3}
B_0/B_{SW}	3	1-10
B_{SW}	5.7 nT	4.275-7.125 nT
τ	1	1-3
C_{10}	1.972	1-2.5

. f_1 primarily affects the expansion and distortion of the cross section whereas f_2 applies to the axis. No rigorous observational studies have yet been done that could constrain the initial expansion velocities in different directions so the fs are free to vary between 0 and 1 and need not vary simultaneously as we may one day find that the axis and cross section behave differently.

4 Ensemble Study Description

To better understand the sensitivity of ANTEATR-PARADE results to the inputs, we perform two-dimensional parameter space explorations for different pairs of input parameters. Table 4 lists the parameters varied as well as the ensemble seed value and the range considered. The ensemble seed values correspond to the seed value from Paper I. For the parameters routinely reconstructed from observations (CME mass M_{CME}, v_F, AW) or measured in situ (1 AU solar wind density n_{SW}, velocity v_{SW}, and magnetic field strength B_{SW}) we use a range representative of the uncertainty in each. Many parameters describe details for which we do not have real constraints ($AW_{\perp}$, the fs and δs, drag coefficient C_d and B_0/B_{SW}) so we consider a plausible range. We pick a range of C_{10} and τ that predominantly yields flux ropes stable to the kink instability.

For each pair of parameters we construct a 21 by 21 grid of ANTEATR-PARADE results, giving us a total of of 3528 simulations for all 8 parameter pairs (M_{CME} and v_F, AW and $AW_{\perp}$, δ_{CS} and δ_{Ax}, δ_{CA} and C_d, f_1 and f_2, v_{SW} and n_{SW}, B_0/B_{SW} and B_{SW}, and τ and C_{10}). For each simulation, we determine 12 output values. Of these, 8 are critical values for space weather predictions - v_F and v_{Exp} at the time of impact, the transit time, the duration, B_t and B_p, and an estimated maximum Kp. The other 4 are of interest as they shed light on the actual physics within the model - δ_{CS}, δ_{Ax}, δ_{CA}, and C_{10}. **We note that we have also looked at changes from the initial radial distance of the CME front, varying it from the seed value of 10 R_S to as low as 5 R_S. We see little sensitivity to this parameter, the largest of which being a slight increase in the travel time as the CME has slightly farther to travel. Most other parameters reach the same equilibrium value by the time they reach 1 AU so we do not include these results in this work.**

The behavior of ANTEATR-PARADE CMEs represents the combination of many different effects. We seek to link changes in various input parameters to changes in the model outputs. Some of our input parameters are also output parameters (e.g. v_F) so there is an obvious direct link. Other outputs are CME properties that evolve with time that are calculated from our inputs (e.g. n from M_{CME}). If the initial value of an output parameter changes then we naturally expect that the final value will as well. This includes changes in the IVD altering the expansion speeds. For these parameters, we will comment whether the variation in the output directly follows the variation in input (e.g. if decreasing the initial δ_{CS} by 0.1 causes the final δ_{CS} to change by 0.1) or if there additional physics-driven effects.

In addition, changes in a input may affect either the drag or magnetic forces that a CME experiences. The background solar wind properties affect only the drag, other than the magnetic field strength that scales the CME magnetic field and factors into the pressure gradient calculation. With the exception of the front velocity, the CME parameters tend to affect both the drag and magnetic forces. As seen in Paper I, the drag forces tend to be stronger than the magnetic forces for our chosen magnetic field model so we can typically attribute most changes to the drag force.

To analyze the ANTEATR-PARADE parameter space exploration we first determine which initial properties are affected by a change in input parameters. We then determine the relative importance of changes in the drag and magnetic forces.

5 Ensemble Study Results

Figures 1-3 show contours of the results of the ANTEATR-PARADE parameter space exploration, grouped by output parameter. Each show results for four outputs with each parameter having its own subplot index (a, b...). The eight panels show the eight different input parameter pairs with the top row showing M_{CME} and v_F, AW and $AW_\perp$, f_1 and f_2, and δ_{Ax} and δ_{CS}, and the bottom row showing τ and C_{10}, B_0/B_{SW} and B_{SW}, v_{SW} and n_{SW}, and δ_{CA} and C_d, from left to right. All contours show the change in an output with respect to the ensemble seed value, which are shown in Table 5. For a single output value, all panels use the same color scale with red corresponding to an increase and blue to a decrease. The yellow star indicates the location of the ensemble seed within each panel.

We determine the maximum increase and decrease in each output that results from changes in a single parameter (i.e. variations along a constant vertical or horizontal line intersecting the star in the contour panels). We use the same ranges as shown in the figures and our identification of most sensitive input parameter will depend on their chosen ranges. Typically the maximum variations occur at the edge of these ranges, though we do find exceptions. Table 5 lists these variations and the corresponding single input parameter. We note that variations of multiple parameters can lead to larger changes than presented in Table 5. **For C_{10}, we only consider values that correspond to kink stable solutions given the seed value of τ.**

5.1 CME Front Velocity

Figure 1(a) shows the change in the velocity of the CME front, v_F. For the final v_F, ANTEATR-PARADE shows a strong sensitivity to the CME mass, initial v_F, drag coefficient, solar wind density and velocity, and, to a lesser extent, both angular widths. Kay et al. (2020) saw a similar dependence on these parameters for the transit time from the original ANTEATR. The final v_F depends on the initial v_F but the variation in the final value is not as large as the initial variation as the drag force changes to negate some of it.

Table 2. Ensemble Seed Output Values

Output	Value	Max. Inc.	Input	Max. Dec.	Input
v_F	710 km/s	230 km/s	δ_{CA}	-170 km/s	M_{CME}
v_{Exp}	94 km/s	37 km/s	f_1	-52 km/s	δ_{CS}
Transit Time	42.5 hr	16.6 hr	v_F	-8.2 hr	v_F
Duration	18.6 hr	6.8 hr	$AW_\perp$	-8.4 hr	B_0/B_{SW}
B_t	7.7 nT	19.3 nT	B_0/B_{SW}	-5.8 nT	τ
B_p	5.8 nT	13.8 nT	B_0/B_{SW}	-4.1 nT	τ
C_{10}	2.17	1.03	B_0/B_{SW}	-0.41	τ
δ_{CS}	0.47	0.34	f_1	-0.25	δ_{CS}
δ_{Ax}	0.42	0.22	f_2	-0.17	f_2
δ_{CA}	0.20	0.07	f_1	-0.07	δ_{CA}
n	10.5 cm^{-3}	31.3 cm^{-3}	AW$_{CS}$	-6.4 cm^{-3}	M_{CME}
Kp	6.5	2.1	B_0/B_{SW}	-2.6	τ

Previously unseen for the original ANTEATR, we also see a strong dependence on δ_{CA}. The ratio of the cross section size to axis size does affect the magnitude of the axial magnetic forces but, more importantly, δ_{CA} affects the total volume of the CME. The volume varies proportionally with δ_{CA} and since we consider a constant mass for each case, so does the density. Large changes with δ_{CA} tend to be representative of the acceleration changing in response to the density, rather than a change in the actual forces.

Many changes in v_F result from changes to the drag force. Changing the drag coefficient by 0.5 can increase v_F by 200 km/s or decrease it by 100 km/s. Changing the CME mass by 50%, which changes the acceleration for a constant force, either drag or magnetic, causes v_F to change by about 150 km/s and is responsible for the largest decrease in v_F. Increasing either angular width increases the area used to calculate the drag force, but we find less sensitivity than seen for C_d or M_{CME}. **An decrease of 10° in AW causes a increase of v_F by 120 km/s. Changing $AW_\perp$ by 5° causes v_F to increase by 50 km/s. Interestingly, our seed values for this CME are such that the chosen $AW_\perp$ produces the minimum v_F. As $AW_\perp$ increases, the drag force increases and the density decreases. Lower density increases the deceleration from drag, but also the expansion of the cross section from internal magnetic forces. Our parameters are just such that as $AW_\perp$ increases the effects of additional expansion dominate and increase v_F and as $AW_\perp$ decreases then weaker drag dominates and v_F increases.** The background solar wind properties also influence the drag forces and v_F. Increasing v_{SW} by 25% increases v_F by 120 km/s, and increasing n_{SW} by 25% decreases v_F by 60 km/s. We find even larger effects when changes in multiple drag force parameters are combined, for example high initial v_F and CME mass can cause changes well over 200 km/s in the final v_F.

The final v_F is less sensitive to the magnetic field model and the IVD. Doubling the CME magnetic field strength relative to the B_{SW} causes v_F to decrease by 50 km/s due to deceleration from the stronger axial magnetic tension force. We see very little other sensitivity to the internal magnetic field model or the initial CME shape. Changing the IVD to either fully self-similar or convective causes a change of less than 100 km/s with the convective cases being slower as they tend to expand more and experience greater drag. Changing a single one of the f parameters that control the IVD by 0.5 causes changes of order 50 km/s in the final v_F.

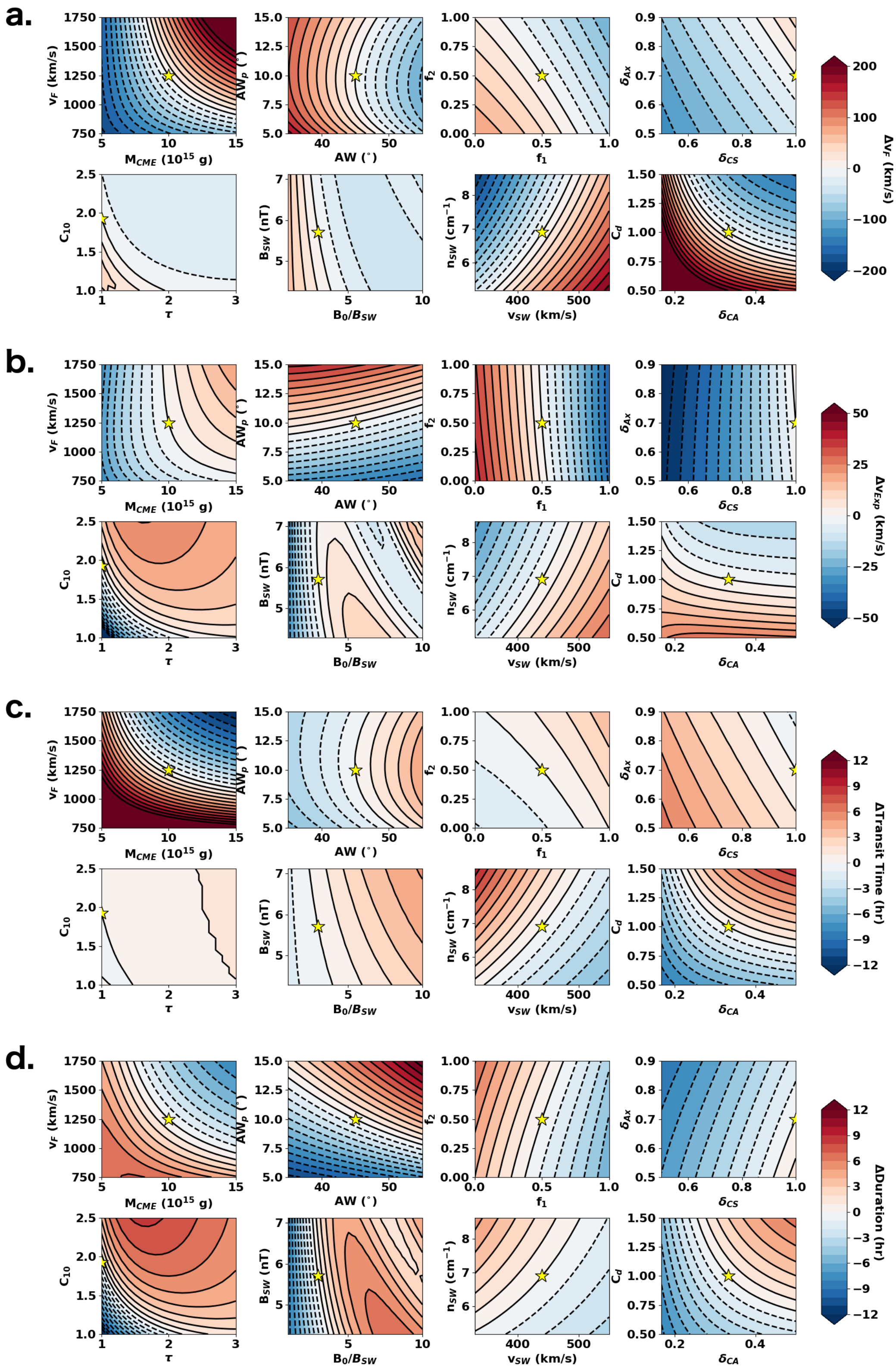

Figure 1. Variations in the different ANTEATR-PARADE outputs for different pairs of input parameters. From top to bottom, Figure 1 shows changes in the velocity of the CME front (a), the CME expansion velocity (b), the transit time (c), and the duration (d). Within each subplot the top row of panels shows from left to right variations with M_{CME} and v_F, AW and $AW_\perp$ (labeled as AW_p in the figure), f_1 and f_2, and δ_{Ax} and δ_{CS}, and the bottom row shows τ and C_{10}, B_0/B_{SW} and B_{SW}, v_{SW} and n_{SW}, and δ_{CA} and C_d. All panels have the same color range for a single output parameter and the yellow star indicates the location of the ensemble seed.

5.2 Expansion Velocity

Figure 1(b) shows the change in v_{Exp}, the expansion speed of the CME's cross section in the radial direction. This is analogous to what would be inferred from in situ observations (up to some geometrical factors accounting for the orientation of an impact). We see changes of at least ±20 km/s within each panel suggesting that the IVD and both forces all contribute to determining the final v_{Exp}. The largest increase and decrease in v_{Exp} come from changes in f_1 and δ_{CS}, respectively, which are used to relate the initial v_F to the initial v_{Exp}.

Changing AW by 5° changes v_{Exp} by less than 5 km/s whereas a 5° change in $AW_\perp$ causes a change of 35 km/s in v_{Exp}. In Section 5.1, we found **that v_F only increases as $AW_\perp$ changes whereas here we see v_{Exp} varies proportionally as $AW_\perp$ changes. These changes in v_{Exp} result from $AW_\perp$ altering the initial expansion velocity and the decrease in density allowing for more expansion of the cross section.**

We also find a strong sensitivity to f_1, which is another important factor in the initial expansion velocity and causes the largest increase in v_{Exp}. The final v_{Exp} for the fully self-similar and fully convective f_1 cases differ by 37 km/s. The strongest decreases in v_{Exp} occur when we decrease δ_{CS}. Decreasing δ_{CS} by 0.5 causes a 52 km/s decrease in v_{Exp}. These changes largely result from the change in the initial v_{Exp} as δ_{CS} factors into the self-similar IVD model, but there are second order effects from δ_{CS} affecting the cross-sectional magnetic forces.

The radial drag force in ANTEATR-PARADE affects both v_F and v_{Exp} so v_{Exp} often behaves similar to v_F. Most drag-induced trends remain the same but the magnitudes may change. Decreases in C_d and M_{CME} cause roughly the same percent change in v_{Exp} as we saw for v_F. These changes appear much weaker in Figure 1(b) than the variations in v_F in Figure 1(a) because other parameters cause even larger variations in v_{Exp}.

Doubling the magnetic field scaling increases v_{Exp} by 10 km/s but decreasing it by half causes a change of 30 km/s. If we continue to increase the scaling by more than a factor of two then v_{Exp} begins to decrease. For these cases, the CME initially expands very rapidly close to the Sun,reaching a quasi-equilibrium state much closer than the CMEs with slightly weaker magnetic field. This allows for more time for the drag forces to slowly decrease v_{Exp} as it continues propagating to 1 AU. This is largely driven by the ratio alone but B_{SW} can also have an effect for larger ratios. This balance between the early rapid expansion and slow, continual drag effects appears for any output parameters that are sensitive to the internal CME magnetic force.

We find that v_{Exp} is also sensitive to the parameters defining the magnetic field model - C_{10} and τ. Most noticeably, increasing C_{10} decreases the poloidal magnetic field and therefore the magnetic tension resisting the expansion of the cross section, leading to smaller v_{Exp}. An increase of 0.5 in C_{10} changes v_{Exp} by 15 km/s. Increasing τ increases the outward pressure gradient force that expands the cross section. An increase of 1 in τ cause a change of 20 km/s in v_{Exp}.

5.3 Transit Time

Figure 1(c) shows the change in the transit time. This is the same Kay et al. (2020) but for the improved model and this work includes results for additional input parameters. We find the strongest sensitivity to the CME velocity. An increase of 500 km/s in v_F causes a 8.2 hr decrease in the time but a decrease of 500 km/s causes a 16.7 hr delay in the transit time. Changing the mass primarily affects the acceleration experienced from the drag force so the behavior is similar to that seen for the output v_F. We see a larger delay from decreasing the mass by 50% (increase of 11.1 hr) as opposed to increasing it by the same amount (decrease of 4.1 hr).

The transit time shows variations of order 5 hr from the combined variations of AW and $AW_\perp$, n_{SW} and v_{SW}, or δ_{CA} and C_d, which also affect the drag. Large magnetic field scaling and B_{SW} can cause a 5 hr increase in the transit time hinting that at very high limits of B_{CME} the axial tension can noticeably decelerate a CME. For all other the parameters the variation in the transit time is less than 5 hr for the ranges we consider.

5.4 Duration

Figure 1(d) shows the variation in the CME duration. The balance between CME expansion and radial deceleration from drag determines the duration as it is a product of the CME size and speed. Accordingly, we expect the behavior of the transit time to mirror that of either v_F or v_{Exp}. Nearly all panels show at least a 5 hr change but the largest **increase of 6.8 hr results from $AW_\perp$, driven by the changes in the initial cross-sectional width and expansion velocity, and the largest decrease of 8.4 hr comes from the ratio of B_0 to B_{SW}, driven by the decrease in expansion from magnetic forces.** We find the same sensitivity of the duration to this ratio as we found for the output v_{Exp}. A decrease in the ratio causes less expansion and shorter duration. An increase in the ratio causes more expansion until we reach the turnover point where excessive overexpansion causes quasi-equilibrium closer to the Sun and the slow, continuous effects of drag have more time to act and the duration begins decreasing.

The effects from other parameters are slightly smaller than but many are of similar magnitude to those from $AW_\perp$ and the magnetic field scaling. Decreasing the CME mass increases the net expansion and overall CME size. A decrease of 50% in M_{CME} causes a 6 hr increase. Decreasing the initial CME velocity decreases the velocity at 1 AU, increasing the duration. A decrease of 500 km/s in v_F corresponds to an increase of 6.4 hr in the duration.

The dependence of the duration on C_{10} and τ is identical to that of v_{Exp} with larger values of either parameter leading to more expansion and longer durations, with changes of about 5 hr. We see some sensitivity to most other input parameters but individual variations tend to cause changes of less than 5 hr in the duration.

5.5 Toroidal Magnetic Field

Figure 2(a) shows the changes in the toroidal magnetic field, B_t. Not surprisingly, we find the strongest sensitivity to the parameters that define the magnetic field model. The largest increase in B_t comes from changing the ratio of B_0/B_{SW}, which will uniformly scale both B_t and B_p. A ratio of 3 was used in Paper I to ensure stability for all the various combinations of magnetic forces and IVD that we considered. Having eliminated the less plausible configurations, the fast CMEs are well-behaved up to much higher ratios. Our chosen range is then antisymmetric as we are not concerned with CMEs weaker than the background solar wind. Increasing the ratio from 3 to 10 causes B_t to increase by 19.3 nT.

In Paper I, the seed values for τ and C_{10} were chosen to most closely mimic a force-free Lundquist flux rope, which is the most commonly used model. For constant τ at the seed value of 1, large decreases in C_{10} can also cause a large increase in B_t but this regime of small τ and C_{10} corresponds to flux ropes that are kink unstable according to Florido-Llinas et al. (2020). The toroidal magnetic field at the center of the flux rope scales linearly with τ so one might expect B_t to also increase. However, increasing τ also increases the outward magnetic pressure gradient and the expansion of the cross section. More ex-

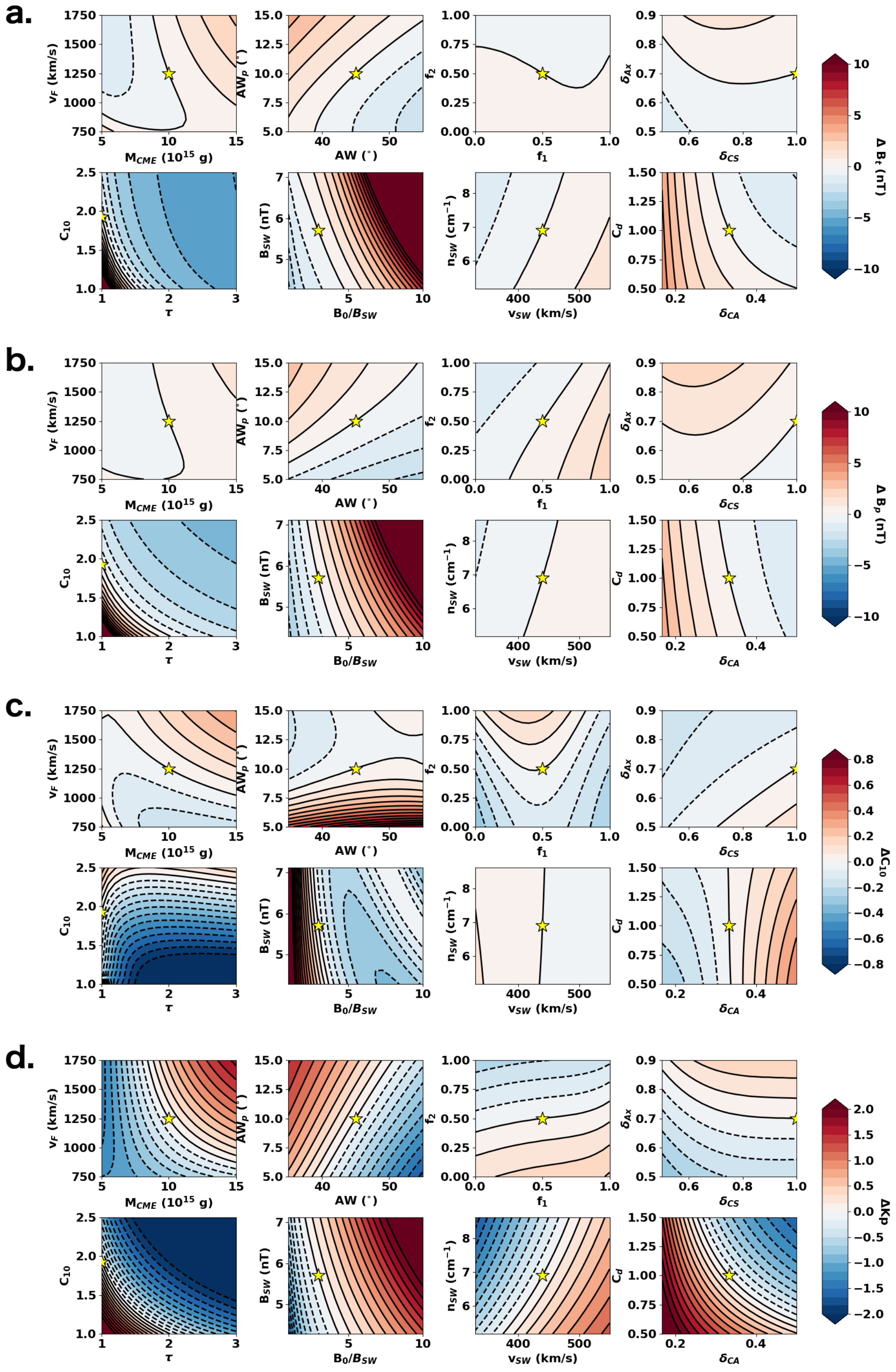

Figure 2. Same as Fig. 1 but showing contours of the change in the output B_t (a), B_p (b), C_{10} (c), and Kp (d).

pansion leads to a weaker B_t by flux conservation. Fig. 2(a) shows that B_t decreases as τ increases, suggesting that the expansion effects must dominate the initial increase in B_t. Increasing τ from 1 to 3 causes B_t to decrease by 5.8 nT.

B_t also depends on δ_{CS} as show in Eq. 2 but we see very little sensitivity to the initial δ_{CS} or any other CME shape parameters, at least relative to the magnetic field model parameters. The largest shape-related changes of 4.4 nT come from decreasing δ_{CA}, which causes smaller denser CMEs that expand less and therefore have B_t decrease less via flux conservation.

We find some dependence on the parameters related to the drag force but these variations are all less than 5 nT for our chosen ranges. In general, as the drag increases the CME has more time to expand during propagation and therefore weaker B_t.

5.6 Poloidal Magnetic Field

Figure 2(b) shows changes in the poloidal magnetic field, B_p. We use the same color scale as for the changes in B_t in Figure 2(a). The behavior is largely the same as that of B_t but with an even weaker dependence on the drag-related parameters. The area for B_t flux conservation depends solely on the cross sectional area perpendicular to the toroidal axis, what we typically refer to as just the cross section, whereas the area for B_p flux conservation depends on the length along the toroidal axis and the radius of the cross section. The drag has less of an effect on the toroidal axis shape and size than it does on the cross section, which leads to less sensitivity for B_p than B_t.

The maximum increase in B_p is again caused by the ratio B_0/B_{SW} with an increase from 3 to 10 causing a 13.8 nT increase. This is about the same change as seen for B_t but for the seed case B_p is about 75% of B_t so this represents a larger percent change in the output. The maximum decrease in B_p comes from increasing τ but the magnitude of the change decreases to 4.1 nT as opposed to 5.8 nT for B_t. τ does not directly scale B_p so this decrease results solely from the changes in CME expansion resulting from the increased magnetic pressure gradient. We continue to see some dependence on δ_{CA} with B_p increasing by 3.5 nT for a decrease of 0.167 in δ_{CS}.

5.7 Magnetic Field Model C_{10}

Figure 2(c) shows changes in the flux rope magnetic field model parameter C_{10}, which inversely scales B_p with respect to the parameter B_0. For the ensemble seed with a τ of 1, a C_{10} below 1.7 will be kink unstable. The seed has a final C_{10} of 2.17 so a decrease of more than 0.47 will correspond to an unstable flux rope. As τ increases, lower values of C_{10} become permissible. The critical C_{10} is 0.75 for a τ of 3, but all ensemble members use a τ of 1 except for those in the τ versus C_{10} panel.

Nearly all of our parameter space variations remain kink stable. We find that changing the initial C_{10} causes a roughly comparable change in the final C_{10}. As τ increases, the final C_{10} becomes slightly more sensitive to the initial C_{10}, but a larger range of initial C_{10} values become permissible due to the change in the kink instability limit.

We also find large increases in the final C_{10} for small initial $AW_{\perp}$, but little sensitivity to increases from our seed value. This increase in C_{10} is not mirrored by as noticeable of a decrease in B_p so the effects must mostly be balanced out by the changes in B_0 and δ_{CS}.

Excessive cross-sectional expansion relative to the expansion of the toroidal axis causes B_t to decrease faster than B_p. We have chosen τ to remain constant so B_0 must decrease to account for the change in B_t, so C_{10} must decrease or B_p will decrease as fast as B_t. We do not have any real justification for holding τ constant rather than varying both it and B_0 but the model is under-constrained by flux conservation alone so we have begun with the simplest approach. With a different choice of initial C_{10} and τ or a different approach to flux conservation we may find different limits on which input parameters yield kink stable flux ropes.

5.8 Maximum Kp

Figure 2(d) shows the maximum estimated Kp. As in Paper I and Kay et al. (2020), we calculate the Kp as

$$Kp = 9.5 - \exp\left[2.17676 - 0.000052 v_F^{4/3} B_\perp^{2/3} \sin^{8/3}\frac{\theta_C}{2}\right] \tag{7}$$

which is based on the empirical expression in Mays et al. (2015). $B_\perp$ is the perpendicular component of the magnetic field in Geocentric Solar Magnetospheric coordinates. θ_C is the clock angle of the magnetic field so that the sine term is maximized for fully southward magnetic field. We use B_p in place of $B_\perp$ and replace the sine term with 1 so that our estimated value is the maximum possible upon initial arrival of the CME front.

Based on the empirical expression, we expect Kp to be sensitive to any inputs that affect v_F or B_p. Since v_F depends mostly on the drag force and B_p depends mostly on the magnetic force, we find that Kp is sensitive to most of our input parameters. Sections 5.1 and 5.6 show larger percentage changes in B_p than v_F so we find that Kp varies more strongly with parameters related to B_p and the magnetic expansion rather than v_F and the drag. Increasing τ from 1 to 3 causes the Kp to decrease by 2.6 due to the decrease in B_p. Decreasing C_{10} causes a large increase in Kp but only when the magnetic field model reaches the kink unstable regime. We see a comparable increase when the ratio B_0/B_{SW} increases, finding an increase of 2.1 for a ratio of 10. **We also finad a strong dependence on δ_{CA}, which can create an increase of 2 or decrease of 1 in Kp due to the changes that results from the effects on the initial density.**

The parameters related to the drag force produce weaker changes but they are not unimportant. For our ranges, changing either the CME mass, velocity, or AW can cause a change of roughly ± 1 in Kp. The background solar wind parameters are weaker but most can still produce changes of 0.5 in the Kp.

5.9 CME Density

Figure 3(c) shows the change in the number density that would be measured in situ at 1 AU. This value depends on the CME mass and the CME volume so we find some sensitivity to many input parameters. Changing the CME mass has a large effect on the number density as expected. Increasing the mass by 50% causes a 9.2 cm^{-3} increase in n. The ensemble seed has a density of 10.5 cm^{-3} so the change in the final density is proportionally larger than the change in the initial mass. This results from the larger density reducing the acceleration from the magnetic forces and less expansion during propagation.

We actually find larger increases from the parameters related to the size, specifically those affecting the initial size and the magnetically-driven expansion. As either initial angular width or δ_{CS} decrease the initial number density increases. The largest increases come from changing $AW_\perp$ with a 5° change causing a 31.3 cm^{-3} increase in n. The effects from δ_{CS} are also strong with an 0.5 decrease causing the density to increase by 11.6 cm^{-3}.

The other parameters related to the magnetic and drag forces have much weaker effects on the final density with most causing changes of no more than 3 cm^{-3}.

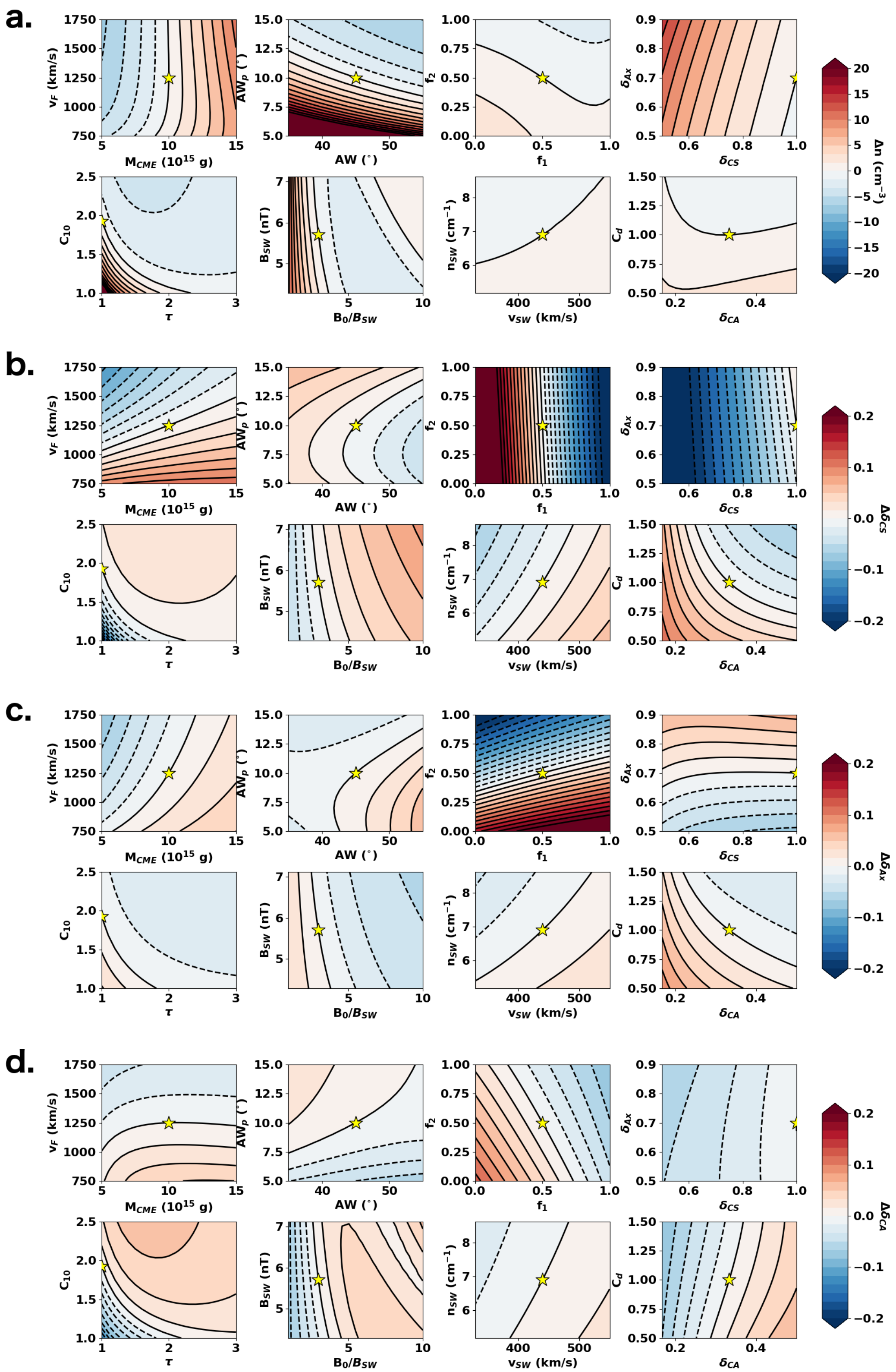

Figure 3. Same as Fig. 1 but showing contours of the change in the output n (a), δ_{CS} (b), δ_{Ax} (c), and δ_{CA} (d).

5.10 CME Cross-Sectional Shape

The remaining three panels show the sensitivity of the various δ parameters describing the shape. The δ themselves are not of particular interest for space weather forecasting and hard to measure from in situ profiles. However, seeing how they are affected will provide better understanding of the fundamental nature of CMEs in interplanetary space.

Figure 3(b) shows the changes in δ_{CS}, the ratio of the width of the cross section in the radial direction to the width of the cross section in the perpendicular direction. The cross section is constantly expanding but δ_{CS} will only change if the widths do not change proportionally. In Paper I we saw that our chosen parameterization of the magnetic field model produces forces that cannot change the cross-sectional shape on their own. Instead the difference between the drag in different directions induces an asymmetry. The magnetic forces still factor into the shape as the net expansion is the difference between the outward magnetic and the inward drag forces. As the magnetic forces increase the asymmetry of the drag forces becomes less important. Since both forces and the IVD have an effect, most inputs can affect the final δ_{CS} to some extent.

The decrease in the final δ_{CS} result from the initial δ_{CS}. A change of 0.5 in the initial δ_{CS} causes a change of 0.25 in the final value. This means that the change in the forces counteracts some of the change in the initial value. Since our forces consistently cause a decrease in δ_{CS} during propagation the forces must become weaker for smaller initial δ_{CS} causing the net decrease between the initial and final values to be smaller.

We see a strong dependence on the IVD, but only through f_1 as that sets the cross-sectional expansion speeds. Increasing f_1 to fully convective-like causes δ_{CS} to decrease by 0.23 whereas δ_{CS} increases by 0.34 by decreasing f_1 to fully self-similar-like.

The dependence of δ_{CS} on B_0/B_{SW} is similar to what we saw for v_{Exp} as these outputs are linked via the expansion. More expansion makes the asymmetry of the drag force less important so δ_{CS} remains higher and more circular. We find much decreases for magnetic field ratios that lead to less expansion overall or excessive early expansion letting drag dominate over longer distances. **We also find a moderate dependence on v_F and δ_{CA}, with both creating increases of order 0.1 in δ_{CS}.** The dependence on the other input parameters is weaker but when the drag force increases, δ_{CS} decreases as the cross section becomes more elliptical.

5.11 CME Axial Shape

Figure 3(c) shows contours of δ_{Ax} using the same color range as δ_{CS} in Fig. 3(b). Most parameters show changes of less than 0.05 in δ_{Ax}. In Paper I, we found little change in δ_{Ax} for different magnetic forces. We saw more sensitivity to the drag, but the effects were still relatively small. The only significant difference resulted from changes in the IVD model.

These 2D parameter space explorations reproduce the effects we found before. None of the parameters that effect the magnetic or drag force cause noticeable changes in δ_{Ax}. The only significant changes results from changing f_2, which affects the IVD, or δ_{Ax}, which affects both the initial value of δ_{Ax} and the IVD. We find the strongest sensitivity to f_2 with increasing to fully self-similar-like (f_2 of 0) causing an increase of 0.22 in the final δ_{Ax}. Decreasing f_2 to fully convective-like causes a decrease of 0.17 in δ_{Ax}. **We also see that δ_{CA} and M_{CME} can have a small effect since they change the CME density and the effectiveness of the forces, but these only cause changes of 0.5 in the final δ_{Ax}**

5.12 CME Cross Section/Axial Ratio

Figure 3(d) shows the ratio of the width cross section in the radial direction to the width of the axis in the perpendicular direction. Again, we use the same contour levels as the other two δ shape parameters. We see less sensitivity to f_1 and f_2 than we did for the other δs but similar weak dependencies on most other parameters. While weaker than the changes in the other δ, the largest changes of 0.07 still come from changing f_1 to either fully convective or full self similar. We also find a decrease of 0.07 in the final δ_{CA} if we decrease the initial δ_{CA} by 0.167, which shows that the change in the forces must counteract the initial change.

6 Ranking Sensitivity

In Section 5 we analyzed which inputs cause the most meaningful changes for each individual output parameter of ANTEATR-PARADE. Ideally, we would like to determine which inputs are the most important to know precisely for accurate space weather predictions. If we could identify one or two that are the most critical then observational studies could begin focusing on how to better constrain these values. To simultaneously compare the importance of different inputs for different outputs, we scale the absolute change in an output by the maximum absolute change of that output for any variation in a single output parameter. Let x_i be the value of an input i that produces the maximum change in some output O_j. For every x_i we have the corresponding maximally varying output $O_j(x_i)$. We define the maximum $O_j(x_i)$ for all i as ΔO_j. We then define the sensitivity of an output j to input i as

$$sens_{ij} = \frac{O_j(x_i) - O_j(x_0)}{\Delta O_j} \tag{8}$$

where x_0 corresponds to the ensemble seed value of x_i. While this allows us to compare the relative importance of inputs to output, we note that it removes all knowledge of the actual magnitude of the change O_j. For example, we find the maximum possible sensitivity of 1 for the output δ_{Ax} on the input f_2, but the maximum change in δ_{Ax} is not particularly large and we would not expect this level of variation to make a significant difference in any space weather predictions. We include the sign of the sensitivity to indicate the direction of change in the output value but this yields no information about whether that results from an increase or decrease in that input parameter. Finally, we note that O_j and the resulting sensitivities are dependent on our chosen ranges for each input value. While there are many caveats to keep in mind, this method allows us a manner of comparing the relative importance of the different input parameters.

6.1 Fast Results

Figure 4(a) shows the sensitivity for the fast CME we presented in Section 5. The vertical axis shows the 16 different input parameters, the horizontal axis shows the 11 output values, and each cell is colored according to the sensitivity. Every column has at least a single cell with a sensitivity of either 1 (dark red/brown) or -1 (dark blue), indicating which input that creates the largest change in that output. These cells correspond to the input parameters listed in Table 5. If there are other parameters that have nearly the same sensitivity as the maximal ones these values will appear noticeably red or blue in Fig. 4(a) whereas the less sensitive ones will be nearly white.

Fig. 4(a) does not add any new information beyond the results of Sec 5 but it does allow us to visualize the sensitivity more easily. We see that inputs closely linked to the drag force (M_{CME}, v_F) affect the transit time and v_F. The magnetic inputs (mostly B_0/B_{SW} but to some extent τ and C_{10}) affect the amount of expansion and therefore the output

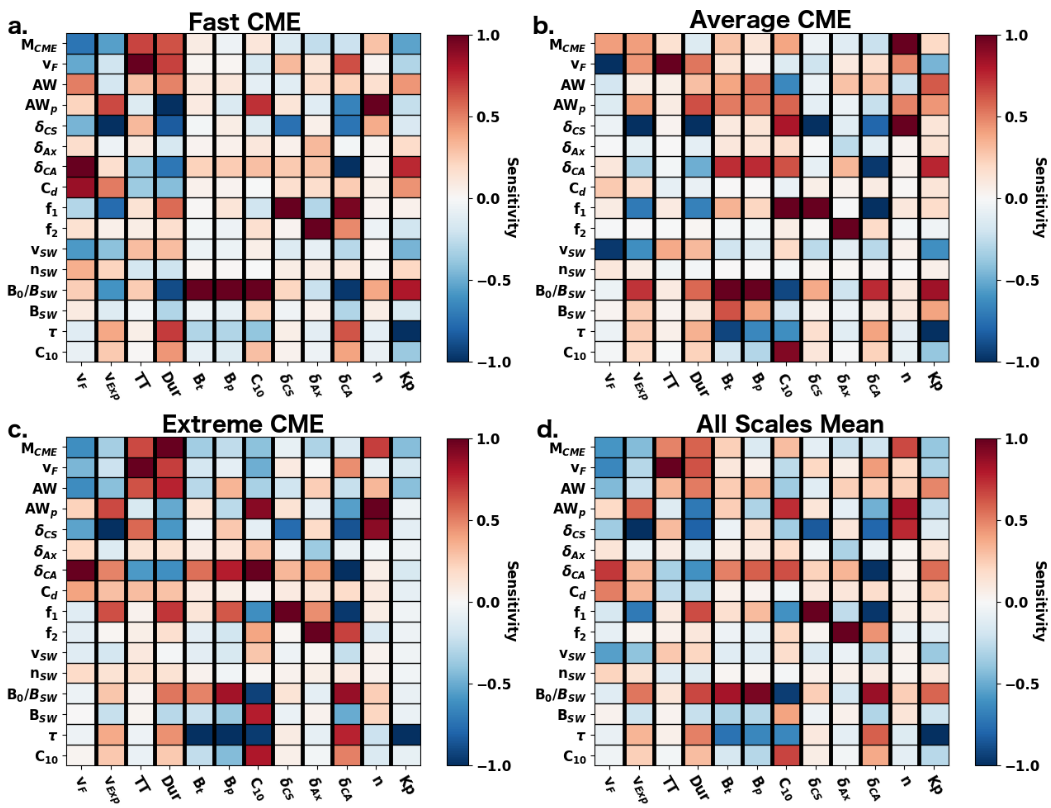

Figure 4. Sensitivity of ANTEATR-PARADE outputs (horizontal axes) to various inputs (vertical axes). We show results for a fast CME (a), average CME (b), extreme CME (c), and a signed mean of all three scales (d).

magnetic properties. The IVD, through the fs and δs, affects the final shape and expansion of the CME, which then determine the duration.

We can also find meaning in the regions with low sensitivity that have the lightest shades in the figure. For example, we do not see a particularly strong dependence on the background solar wind properties for any output other than v_F. **The magnetic field does not depend strongly on much other than the initial scaling of the CME's magnetic field strength. This could help identify which parameters are not top priorities to constrain if one is only concerned with specific outputs.**

Any quantitative analysis of the sensitivity will involve some what arbitrary criteria but it is the only manner by which we can attempt to rank the importance of the various inputs. We set a cutoff for "importance" by determining which inputs can cause variations $\geq$50% of their ΔO_j. We have 192 unique pairs of inputs and outputs and find that 41 of them satisfy this criteria for importance. The most important is B_0/B_{SW}, which satisfies our criteria for 7 outputs, followed by M_{CME} and $AW_\perp$ (5), v_F, δ_{CS}, δ_{CA} (4), and f_1 (5) and τ (3). We do not list the inputs with 2 or fewer important sensitivities.

B_0/B_{SW}, $AW_\perp$, δ_{CS}, δ_{CA}, and $f_!$ are some of the least constrained inputs with the largest ranges of possible values. This very well may be the sole reason that they produce the largest ranges in outputs rather than the sensitivity of the underlying physics. However, these ranges are meant to be representative of our current limits of understanding so regardless of the source of the sensitivity we can say that improving our constraints on these values will be the most effective way to improve the uncertainty in the ANTEATR-PARADE outputs.

6.2 Other Scale CMEs

We have repeated the simulations of Sec. 5 using the average and extreme CMEs from Paper I as ensemble seeds. Figure 4(b) shows the sensitivities for the average case and Figure 4(c) shows the sensitivities for the extreme case. We can immediately see that there are noticeable differences between CMEs of different strengths.

For example, we consider the duration. The fast CME shows the strongest dependence on $AW_\perp$ and δ_{CS} with weaker but non-negligible dependencies on M_{CME}, v_F, δ_{CA}, B_0/B_{SW}, and τ. If we look at the duration for the average CME we see a much weaker dependence on most input parameters. $AW_\perp$ and δ_{CS} still dominate the changes in the duration but there are less effects from the others. The slow CME moves at nearly the background solar wind speed so there are fewer drag effects. It also has weaker magnetic expansion so the duration is essentially dominated by the values that determine the initial size. For the average CMEs we consistently see a strong dependence on the initial values and less variation from drag and magnetic forces.

In contrast, the extreme CME retains many of these dependencies of the fast CMEs but the relative importance changes with M_{CME} becoming the most important. We also see an increase in sensitivity to AW and f_1 from the fast case. For some parameters, such as δ_{Ax}, the sign of the sensitivity changes. We emphasize that this is not a reversal in how the duration varies with δ_{Ax}, rather that we see a larger decrease than increase in the duration for the extreme CME whereas the fast CME shows a larger increase. In general, we find that the extreme CME tends to have enhanced sensitivity to the parameters related to drag since the differential speed between the CME and background solar wind is much larger for this case. We still find some sensitivity to the parameters related to the magnetic force, though typically less than for the fast case.

Using our criteria for importance, we find that the average CME also depends most strongly on B_0/B_{SW} (7 outputs), followed by δ_{CS} (6), δ_{CA} and

f_1 (5), $AW_\perp$ and τ (4), and v_F, AW, and v_{SW} (3). For the extreme sensitivity, the most important inputs are δ_{CS}, δ_{CS}, and f_1 (7 outputs each) followed by τ and $AW_\perp$ (5), M_{CME} and B_0/B_{SW} (4), and AW (3). This show that different scale CMEs are most sensitive to different inputs.

To illuminate any universal trends across different CME scales we take the mean of the absolute value of the sensitivity for all three scales. We then assign it the dominant sign of the three cases and plot this as the all scales mean in Figure 4(d). We see a few points where a input consistently cause at least 90% of the maximum change in an output, specifically variations in the transit time from v_F, δ_{CS} and δ_{CA} from f_1, δ_{Ax} from f_2, B_p and C_{10} from B_0/B_{SW}, and the Kp from τ. We find 16 instances with a mean sensitivity of greater than 75% with δ_{CS} and B_0/B_{SW} being responsible for 9 of them. Lowering the criteria to 50% yields an total of 45 pairs with 34 of the having either $AW_\perp$, δ_{CS}, δ_{CA}, f_1, B_0/B_{SW}, or τ as the input. Accordingly, we suggest that space weather predictions of the outputs considered here can best be improved by improving our measurements of $AW_\perp$, δ_{CS}, δ_{CA}, f_1, B_0/B_{SW}, or τ.

7 Discussion

While this paper represents represents the most comprehensive study of the sensitivity of space weather parameters related to CME propagation, we by no means have fully resolved their dependencies. Most noticeably, we have considered the simplest version of the Nieves-Chinchilla et al. (2018) magnetic field model using [m,n] = [0,1], which produces no asymmetry in the magnetic forces causing cross-sectional expansion. It remains to be seen if magnetic forces could induce stronger effects with a different magnetic field model. The magnetic forces must be re-derived for different combinations of m and n (or a generic expression derived, if possible), which will be the focus of a future study. Additionally, other effects may cause more extensive changes in a CME's magnetic field than simple distortion of the cross section. For example, magnetic erosion eats away at one side of a flux rope (e.g Ruffenach et al., 2012, 2015) , which should cause asymmetries in the magnetic forces. As with the rest of the OSPREI suite, ANTEATR-PARADE has a very modular design making it simple for future work to replace the magnetic field model or add additional forces affecting the CME's propagation.

We suggest that ANTEATR-PARADE could provide new insights into the behavior of CMEs close to the Sun. We can easily constrain an input by matching the simulation results to a single observable, but this may not reduce things below the plausible range one would guess based on previous observational studies or common sense intuition, especially if there is uncertainty in the observable output. We may be able to significantly tighten our constraints by forcing the results to simultaneously reproduce multiple observables. For example, δ_{CS} is nearly impossible to measure in the corona but we see that v_{Exp} and the duration are fairly sensitive to it for all CMEs. We identified several parameters, most of which are hard to measure in the corona, as the most crucial for improving space weather predictions because they affect the largest number outputs of ANTEATR-PARADE. This means, however, that we have the most opportunities to constrain them for specific events using in situ observations, and hopefully develop general trends that could be applied to future predictions.

8 Conclusion

We present a parameter space study for the new ANTEATR-PARADE model, determining how each input affects each of the outputs. This model is one of the most comprehensive interplanetary CME propagation models so the outputs are not limited to the transit time and CME velocities upon impact, but also include the magnetic properties of the CME, the CME shape, and an estimated Kp index. If we can identify the inputs that cause the largest variations in the outputs then future space weather predictions could be improved by focusing on refining our ability to measure those specific inputs.

The variations can be attributed to either changes in the initial values of certain output parameters, to changes in the drag force that decelerates the CME, or to changes in the magnetic force which expands the CME cross section. We first consider a fast CME. We find that parameters related to the drag force affect the final front velocity of the CME and transit time whereas parameters related to the magnetic forces affect the cross-sectional expansion and therefore the final expansion speed and internal magnetic properties. Both the CME duration and estimate Kp combine the effects of drag and magnetic expansion and show sensitivity to many input parameters.

We extend our analysis to an average CME moving slightly faster than the background solar wind and an extreme CME that moves much faster. The effects of drag become more important for the extreme CME and weaker for the average CME. In contrast, the magnetic forces become more important for the average CME and weaker for the extreme CME. We define a metric to quantify the sensitivity of each output to each input. The sensitivities noticeably vary between the average, fast, and extreme CMEs. We find that over all scale CMEs the largest sensitivities tend to occur for the parameters defining the internal magnetic field model, the size and shape of the CME cross section, and the precise manner in which the initial expansion velocities are defined. While still important, we see weaker sensitivity to the properties of the background solar wind and the size and shape of the CME's central axis. These trends are specific to ANTEATR-PARADE with the current magnetic field model, but further study may confirm their importance for space weather predictions in general.

Acknowledgments

CK is supported by the National Aeronautics and Space Administration under Grant 80NSSC19K0274 issued through the Heliophysics Guest Investigators Program and by the National Aeronautics and Space Administration under Grant 80NSSC19K0909 issued through the Heliophysics Early Career Investigators Program. The ANTEATR-PARADE code is archived through Zenodo at doi:10.5281/zenodo.4279860

References

Al-Haddad, N., Nieves-Chinchilla, T., Savani, N. P., Lugaz, N., & Roussev, I. I. (2018, May). Fitting and Reconstruction of Thirteen Simple Coronal Mass Ejections. *Solar Physics*, *293*(5), 73. doi: 10.1007/s11207-018-1288-3

Amerstorfer, T., Möstl, C., Hess, P., Temmer, M., Mays, M. L., Reiss, M. A., ... Bourdin, P. A. (2018, July). Ensemble Prediction of a Halo Coronal Mass Ejection Using Heliospheric Imagers. *Space Weather*, *16*(7), 784-801. doi: 10.1029/2017SW001786

Baker, D. N. (2000, December). The occurrence of operational anomalies in spacecraft and their relationship to space weather. *IEEE Transactions on Plasma Science*, *28*, 2007-2016. doi: 10.1109/27.902228

Chi, Y., Zhang, J., Shen, C., Hess, P., Liu, L., Mishra, W., & Wang, Y. (2018, aug). Observational study of an earth-affecting problematic ICME from STEREO. *The Astrophysical Journal*, *863*(1), 108. Retrieved from `https://doi.org/10.3847%2F1538-4357%2Faacf44` doi: 10.3847/1538-4357/aacf44

Dumbović, M., Čalogović, J., Vršnak, B., Temmer, M., Mays, M. L., Veronig, A., & Piantschitsch, I. (2018, February). The Drag-based Ensemble Model (DBEM) for Coronal Mass Ejection Propagation. *The Astrophysical Journal*, *854*, 180. doi: 10.3847/1538-4357/aaaa66

Florido-Llinas, M., Nieves-Chinchilla, T., & Linton, M. G. (2020, July). Analysis of the Helical Kink Stability of Differently Twisted Magnetic Flux Ropes. *arXiv* *e-prints*, arXiv:2007.06345.

Gopalswamy, N., Yashiro, S., Akiyama, S., & Xie, H. (2017, April). Estimation of Reconnection Flux Using Post-eruption Arcades and Its Relevance to Magnetic Clouds at 1 AU. , *292*(4), 65. doi: 10.1007/s11207-017-1080-9

Hess, P., & Zhang, J. (2015, October). Predicting CME Ejecta and Sheath Front Arrival at L1 with a Data-constrained Physical Model. *The Astrophysical Journal*, *812*, 144. doi: 10.1088/0004-637X/812/2/144

Isavnin, A. (2016, December). FRiED: A Novel Three-dimensional Model of Coronal Mass Ejections. *The Astrophysical Journal*, *833*, 267. doi: 10.3847/1538-4357/833/2/267

Jin, M., Manchester, W. B., van der Holst, B., Sokolov, I., Tóth, G., Vourlidas, A., … Gombosi, T. I. (2017, January). Chromosphere to 1 AU Simulation of the 2011 March 7th Event: A Comprehensive Study of Coronal Mass Ejection Propagation. *The Astrophysical Journal*, *834*, 172. doi: 10.3847/1538-4357/834/2/172

Kay, C., & Gopalswamy, N. (2018, Sep). The Effects of Uncertainty in Initial CME Input Parameters on Deflection, Rotation, B_z, and Arrival Time Predictions. *Journal of Geophysical Research (Space Physics)*, *123*(9), 7220-7240. doi: 10.1029/2018JA025780

Kay, C., Gopalswamy, N., Reinard, A., & Opher, M. (2017, February). Predicting the Magnetic Field of Earth-impacting CMEs. *The Astrophysical Journal*, *835*, 117. doi: 10.3847/1538-4357/835/2/117

Kay, C., Mays, M. L., & Verbeke, C. (2020, January). Identifying Critical Input Parameters for Improving Drag-Based CME Arrival Time Predictions. *Space Weather*, *18*(1), e02382. doi: 10.1029/2019SW002382

Kay, C., & Nieves-Chinchilla, T. (2020, November). Modeling Interplanetary Expansion and Deformation of CMEs with ANTEATR-PARADE I: Relative Contribution of Different Forces. *arXiv e-prints*, arXiv:2011.06030.

Kay, C., Opher, M., & Evans, R. M. (2015, June). Global Trends of CME Deflections Based on CME and Solar Parameters. *The Astrophysical Journal*, *805*, 168. doi: 10.1088/0004-637X/805/2/168

Kunkel, V., & Chen, J. (2010, June). Evolution of a Coronal Mass Ejection and its Magnetic Field in Interplanetary Space. *The Astrophysical Journal Letters*, *715*, L80-L83. doi: 10.1088/2041-8205/715/2/L80

Liu, J., Ye, Y., Shen, C., Wang, Y., & Erdélyi, R. (2018, March). A New Tool for CME Arrival Time Prediction using Machine Learning Algorithms: CAT-PUMA. *The Astrophysical Journal*, *855*, 109. doi: 10.3847/1538-4357/aaae69

Mays, M. L., Taktakishvili, A., Pulkkinen, A., MacNeice, P. J., Rastätter, L., Odstrcil, D., … Kuznetsova, M. M. (2015, June). Ensemble Modeling of CMEs Using the WSA-ENLIL+Cone Model. *Solar Physics*, *290*, 1775-1814. doi: 10.1007/s11207-015-0692-1

Mierla, M., Inhester, B., Antunes, A., Boursier, Y., Byrne, J. P., Colaninno, R., … Zhukov, A. N. (2010, January). On the 3-D reconstruction of Coronal Mass Ejections using coronagraph data. *Annales Geophysicae*, *28*, 203-215. doi: 10.5194/angeo-28-203-2010

Möstl, C., Rollett, T., Frahm, R. A., Liu, Y. D., Long, D. M., Colaninno, R. C., … Vršnak, B. (2015, May). Strong coronal channelling and interplanetary evolution of a solar storm up to Earth and Mars. *Nature Communications*, *6*, 7135. doi: 10.1038/ncomms8135

Nieves-Chinchilla, T., Colaninno, R., Vourlidas, A., Szabo, A., Lepping, R. P., Boardsen, S. A., … Korth, H. (2012, June). Remote and in situ observations of an unusual Earth-directed coronal mass ejection from multiple viewpoints. *Journal of Geophysical Research (Space Physics)*, *117*, 6106. doi: 10.1029/2011JA017243

Nieves-Chinchilla, T., Linton, M. G., Hidalgo, M. A., & Vourlidas, A. (2018, July).

Elliptic-cylindrical Analytical Flux Rope Model for Magnetic Clouds. , *861*(2), 139. doi: 10.3847/1538-4357/aac951

Odstrcil, D., Pizzo, V. J., Linker, J. A., Riley, P., Lionello, R., & Mikic, Z. (2004, Oct). Initial coupling of coronal and heliospheric numerical magnetohydrodynamic codes. *Journal of Atmospheric and Solar-Terrestrial Physics*, *66*(15-16), 1311-1320. doi: 10.1016/j.jastp.2004.04.007

Owens, M., & Cargill, P. (2004, December). Non-radial solar wind flows induced by the motion of interplanetary coronal mass ejections. *Annales Geophysicae*, *22*(12), 4397-4406. doi: 10.5194/angeo-22-4397-2004

Owens, M. J., Cargill, P. J., Pagel, C., Siscoe, G. L., & Crooker, N. U. (2005, Jan). Characteristic magnetic field and speed properties of interplanetary coronal mass ejections and their sheath regions. *Journal of Geophysical Research (Space Physics)*, *110*(A1), A01105. doi: 10.1029/2004JA010814

Pomoell, J., & Poedts, S. (2018, Jun). EUHFORIA: European heliospheric forecasting information asset. *Journal of Space Weather and Space Climate*, *8*, A35. doi: 10.1051/swsc/2018020

Riley, P., & Crooker, N. U. (2004, January). Kinematic Treatment of Coronal Mass Ejection Evolution in the Solar Wind. *The Astrophysical Journal*, *600*, 1035-1042. doi: 10.1086/379974

Riley, P., Mays, M. L., Andries, J., Amerstorfer, T., Biesecker, D., Delouille, V., … Zhao, X. (2018, Sep). Forecasting the Arrival Time of Coronal Mass Ejections: Analysis of the CCMC CME Scoreboard. *Space Weather*, *16*(9), 1245-1260. doi: 10.1029/2018SW001962

Ruffenach, A., Lavraud, B., Farrugia, C. J., Démoulin, P., Dasso, S., Owens, M. J., … Galvin, A. B. (2015, January). Statistical study of magnetic cloud erosion by magnetic reconnection. *Journal of Geophysical Research (Space Physics)*, *120*(1), 43-60. doi: 10.1002/2014JA020628

Ruffenach, A., Lavraud, B., Owens, M. J., Sauvaud, J. A., Savani, N. P., Rouillard, A. P., … Galvin, A. B. (2012, September). Multispacecraft observation of magnetic cloud erosion by magnetic reconnection during propagation. *Journal of Geophysical Research (Space Physics)*, *117*(A9), A09101. doi: 10.1029/2012JA017624

Russell, C. T., & Mulligan, T. (2002, Apr). On the magnetosheath thicknesses of interplanetary coronal mass ejections. *Planetary and Space Sciences*, *50*(5-6), 527-534. doi: 10.1016/S0032-0633(02)00031-4

Savani, N. P., Vourlidas, A., Szabo, A., Mays, M. L., Richardson, I. G., Thompson, B. J., … Nieves-Chinchilla, T. (2015, June). Predicting the magnetic vectors within coronal mass ejections arriving at Earth: 1. Initial architecture. *Space Weather*, *13*, 374-385. doi: 10.1002/2015SW001171

Schrijver, C. J. (2015, September). Socio-Economic Hazards and Impacts of Space Weather: The Important Range Between Mild and Extreme. *Space Weather*, *13*, 524-528. doi: 10.1002/2015SW001252

Verbeke, C., Mays, M. L., Temmer, M., Bingham, S., Steenburgh, R., Dumbović, M., … Andries, J. (2019, Jan). Benchmarking CME Arrival Time and Impact: Progress on Metadata, Metrics, and Events. *Space Weather*, *17*(1), 6-26. doi: 10.1029/2018SW002046

Vršnak, B., Žic, T., Vrbanec, D., Temmer, M., Rollett, T., Möstl, C., … Shanmugaraju, A. (2013, July). Propagation of Interplanetary Coronal Mass Ejections: The Drag-Based Model. *Solar Physics*, *285*, 295-315. doi: 10.1007/s11207-012-0035-4

Wold, A. M., Mays, M. L., Taktakishvili, A., Jian, L. K., Odstrcil, D., & MacNeice, P. (2018, March). Verification of real-time WSA-ENLIL+Cone simulations of CME arrival-time at the CCMC from 2010 to 2016. *Journal of Space Weather and Space Climate*, *8*(27), A17. doi: 10.1051/swsc/2018005

Xie, H., Ofman, L., & Lawrence, G. (2004, March). Cone model for halo CMEs: Application to space weather forecasting. *Journal of Geophysical Research (Space Physics)*, *109*, 3109. doi: 10.1029/2003JA010226

Xue, X. H., Wang, C. B., & Dou, X. K. (2005, August). An ice-cream cone model for coronal mass ejections. *Journal of Geophysical Research (Space Physics)*, *110*, 8103. doi: 10.1029/2004JA010698